Water Research X 26 (2025) 100293

Contents lists available at ScienceDirect

Water Research X

journal homepage: www.sciencedirect.com/journal/water-research-x

Nanofluid-peroxydisulfate integrated volumetric solar interfacial evaporation system for water evaporation and organic pollutant removal

Chenqi Zhu, Debing Wang, Shiying Bu, Zhichao Wu, Jie Zhang, Qiaoying Wang *

State Key Laboratory of Pollution Control and Resource Reuse, Shanghai Institute of Pollution Control and Ecological Security, College of Environmental Science and Engineering, Tongji University, Shanghai 200092, China

ARTICLE INFO

Keywords:
Peroxydisulfate
Nanofluids
High-salt organic wastewater
Volumetric solar interfacial evaporation

ABSTRACT

Solar evaporation exhibits significant potential for the treatment of high-salt organic wastewater. However, it's also confronted with challenges due to the accumulation of organic pollutants and salts in the concentrated wastewater following evaporation, which compromises the long-term stability of evaporation unit and complicates subsequent treatment processes. To address these challenges, a volumetric solar interfacial evaporation (V-SIE) system by integrating Fe_3O_4–H_2O nanofluids and peroxydisulfate (PDS) were proposed in this study. In V-SIE system, Fe_3O_4 magnetic nanoparticles (NPs) were prepared as solar receivers to form a volume-absorbing solar energy interface and enhance evaporation efficiency. The results show that the evaporation rate was 1.412 kg/(m^2·h) and the solar efficiency reached 93.75 % as the temperature rose to 57.2 ℃. Additionally, the high thermal conductivity of Fe_3O_4 facilitated the effective heat transfer to the fluid and provided sufficient thermal energy to activate PDS, thereby removing 99.3 % of Rhodamine B (RhB). Fe_3O_4 NPs effectively promoted the generation of reactive species including $SO_4^{\cdot-}$, ·OH, $O_2^{\cdot-}$ and $^1O_2$ from PDS and the four main stages including N-de-ethylation, chromophore cleavage, ring-opening, and mineralization were proposed as the possible degradation pathway of RhB. This study provides a reference for developing V-SIE system and highlights the positive effect of nanofluids in advanced oxidation processes.

1. Introduction

With rapid development of industrialization, industries such as petrochemical, printing and dyeing, and pesticide production are producing large amounts of high-salt organic wastewater. The treatment of high-salt wastewater faces significant challenges (He et al., 2023; Chen et al., 2017; Ren et al., 2021), because the traditional biological treatment methods are not well-suited for high-salt conditions (Liu et al., 2024), while the physicochemical treatment technologies including chemical precipitation (Chen et al., 2022), ion exchange (Jia et al., 2023) and reverse osmosis (Wang et al., 2022) are costly, energy-intensive and may cause secondary pollution.

Solar interfacial evaporation (SIE) using photothermal materials can efficiently extract distilled water from wastewater at low cost (Ngoc et al., 2024; Tram et al., 2023), which makes it a great option for tackling water scarcity challenges (Dao et al., 2020; Djellabi et al., 2021; Nguyen et al., 2023). In particular, SIE technology could simultaneously desalinate seawater and treat high-salt wastewater (Irshad et al., 2023; Arshad et al., 2023; Trinh et al., 2022). Typically, high-salt wastewater comprises salts, heavy metals, organic compounds, and even volatile organic compounds (VOCs) (Wang et al., 2018; Wang et al. 2019). Therefore, the temperature rise inevitably leads to the evaporation of harmful substances and accumulation in the condensate during the rapid water evaporation process (Chen et al., 2021; Wang et al., 2023). The reported research mainly focuses on collecting clean water (Qu et al., 2023), critical issues such as the accumulation of high concentrations of organic pollutants, salts, and bacteria in the condensed wastewater after evaporation have been largely ignored. The accumulation of these pollutants makes subsequent post-treatment procedures more challenging and threatens the long-term stability of the evaporation unit. As a result, a dual-function solar evaporator has been developed, utilizing techniques such as adsorption (Chen et al., 2024), photo-Fenton oxidation (Liu et al., 2024), and additional oxidizing agents (He et al., 2023). This system enables the efficient in-situ treatment of high-salt organic wastewater while simultaneously producing clean water (Zhang et al., 2023). However, the heat is concentrated at the upper interface, leading to a lower temperature in the bulking section of reactor, particularly in large-volume reactors (Zhang et al., 2023). This temperature gradient

* Corresponding author.
E-mail address: qywang@tongji.edu.cn (Q. Wang).

https://doi.org/10.1016/j.wroa.2024.100293
Received 7 October 2024; Received in revised form 18 November 2024; Accepted 2 December 2024
Available online 3 December 2024

hinders the effective activation of oxidant. Therefore, optimizing the thermal management of evaporator is a critical aspect that requires careful attention.

Among the techniques mentioned above for the in-situ treatment of high-salt organic wastewater, peroxydisulfate-based advanced oxidation processes (AOPs), are highly effective for treating refractory organic matter due to their high redox potential, extended lifespan, and versatile application at a wide pH range (Hu et al., 2020; Qian et al., 2020). Additionally, previous studies have shown that the reaction of $SO_4^{\cdot-}$ and ·OH with Cl^- leads to the formation of ·Cl and ·ClOH, which play an active role in breaking down pollutants (Li et al., 2022). Importantly, peroxydisulfate (PDS) can also be thermally activated (Mora et al., 2009), which provides the possibility of utilizing the heat management of evaporator to treat organic pollutants accumulation in high-salt organic wastewater. However, SIE technology induces water evaporation through photothermal conversion at the water-air interface, creating a localized thermal zone (Wang et al., 2021). In other words, it concentrates heat energy in a specific area rather than dispersing it throughout the entire body of water. This poses a significant challenge for using the heat from evaporator to activate PDS for degrading organic pollutants, as the persulfate oxidation process requires sufficient activation energy and sustained reaction time (Forouzesh et al., 2021).

Recent advancements have shown that incorporating nanofluids into volumetric evaporation systems can greatly enhance solar evaporation efficiency. This improvement is attributed to the ability of nanoparticles (NPs) to harness solar energy and transform it into thermal energy (Meng et al., 2022). Canh et al. introduced carbon nanodot (CDs) nanofluid to achieve high-rate evaporation of 1.93 kg/(m^2·h) under one sun irradiation (Canh et al., 2024). Wang et al. effectively produced plasmonic nanofluids with gold NPs and showed that these NPs rapidly absorb light and then efficiently transfer the heat into the surrounding fluid. The nanofluids with 178 ppm gold NPs demonstrated a photothermal conversion efficiency of 92.5 %, resulting in a water evaporation efficiency of 65.9 % under standard one-sun illumination (Wang

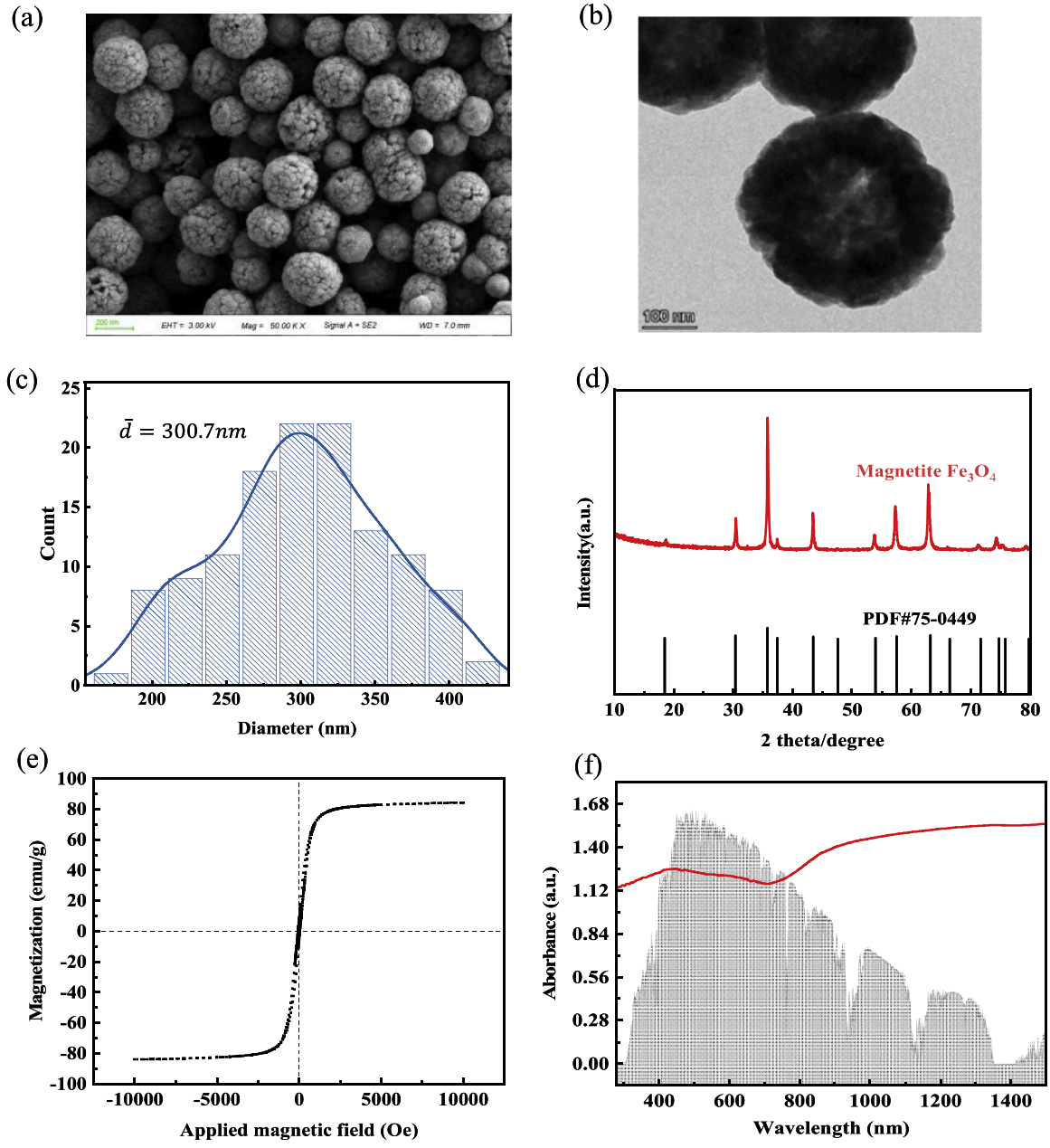

Fig. 1. SEM image (a); TEM image (b); particle size statistics (c); XRD pattern (d); magnetic hysteresis loops (e) and absorption spectrum (f) of Fe_3O_4 NPs.

et al., 2017).

Inspired by these findings, we proposed a volumetric solar interfacial evaporation (V-SIE) system integrating nanofluids and PDS. In this system, concentrated NPs are used to develop a volumetric solar energy absorption interface, maintaining high evaporation efficiency. Simultaneously, the high thermal conductivity of NPs heats the fluid beneath the absorber, providing sufficient thermal energy and reaction time to activate PDS. Herein, magnetic Fe_3O_4 NPs was prepared by solvothermal method as solar receivers. The solar-driven evaporation performance and steam water recovery of the system are firstly discussed in detail. Meanwhile, RhB was chosen as the representative high-salt organic wastewater contaminants to comprehensively examine the degradation mechanism of organic pollutants during its evaporation and concentration process.

2. Results and discussion

2.1. Characteristics of Fe_3O_4 NPs

The SEM images of Fe_3O_4 NPs are shown in Fig. 1(a), which reveal that the samples exhibit regular and spherical shapes with rough surfaces. This uneven pattern enhances the surface area, which is beneficial for catalytic activity. The ultrastructural features (Fig. 1(b)) revealed that the Fe_3O_4 NPs were heterogeneous in size and had a hollow spherical shape. Additionally, the lattice patterns were visible at high resolution, and the average diameter of particles was 300.7 nm (Fig. 1(c)). The results of XRD pattern (Fig. 1(d)) validate the well-defined crystalline structure of synthesized Fe_3O_4 NPs. The clear and distinct peaks in the XRD pattern signify the well-established crystalline structure of particles: 30.4° (220), 35.8° (311), 43.5° (400), 53.9° (422), 57.5° (511) and 63.1° (440), which is in line with the standard card of 75 – 0449. The Fe_3O_4 NPs showed a strong saturation magnetization of 84.0 emu/g, demonstrating their pronounced ferromagnetic property (Fig. 1(e)). The completely reversible M(H) hysteresis loops suggest that the Fe_3O_4 NPs exhibit superparamagnetic behavior (Zhang et al., 2014) and can be effectively separated from the suspension using a magnet. The absorption spectra of Fe_3O_4 NPs in Fig. 1(f) show significant absorption at 200 to 1500 nm, effectively covering the core spectrum of solar radiation. The light absorbance of Fe_3O_4 NPs confirmed by UV–Vis spectra (Fig. S1) was always higher than 85 %.

2.2. Solar-driven evaporation performance

Temperature plays a crucial role in the activation of PDS. When the

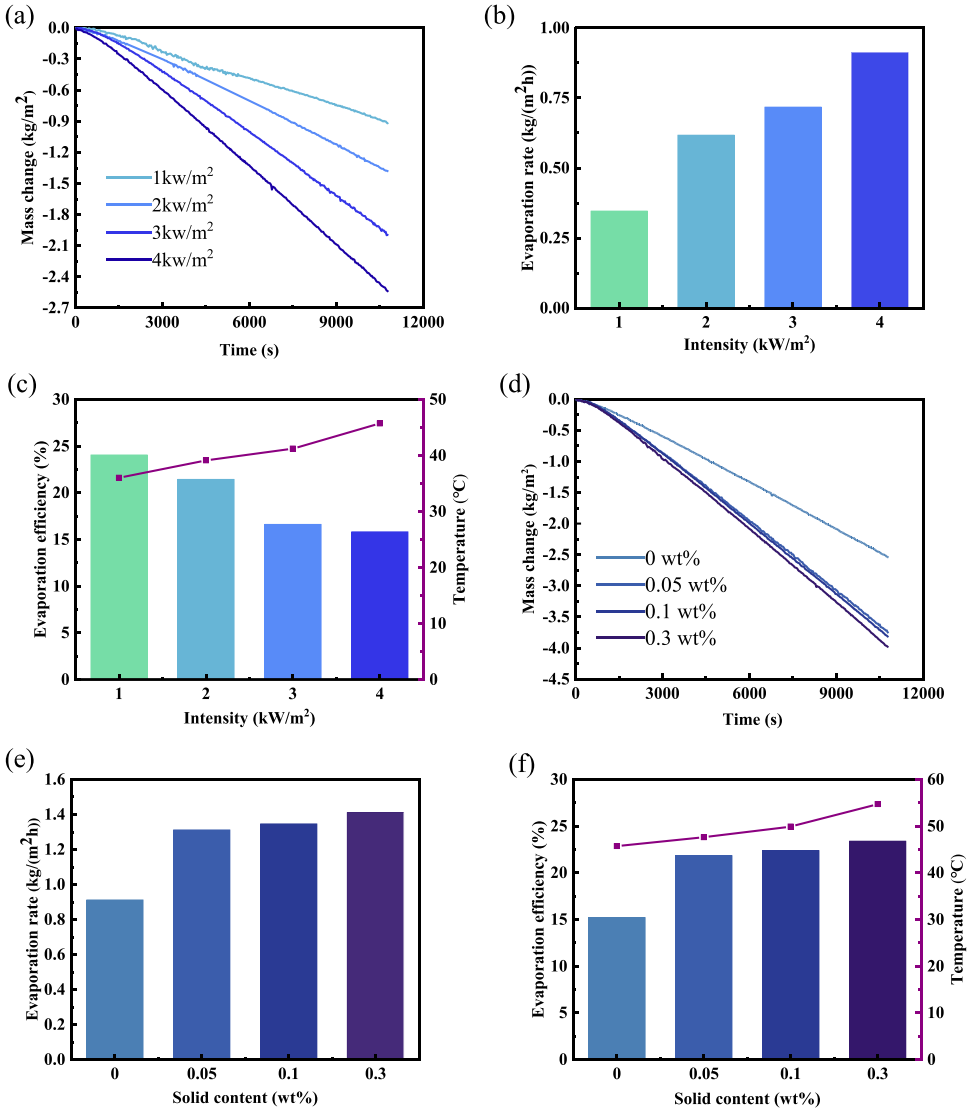

Fig. 2. Mass change (a), evaporation rate (b) temperature and evaporation efficiency (c) of the systems under different light intensity (1, 2, 3 and 4 kw/m^2); mass change (d), evaporation rate (e) temperature and evaporation efficiency (f) of the systems with different Fe_3O_4 concentrations (0, 0.05, 0.1 and 0.3 wt%).

temperature is below 50 °C, the low activation energy of system prevents the cleavage of the O—O bond in PDS, reducing the production of $SO_4^{\cdot-}$. However, with an increase in temperature, the efficiency of degrading organic pollutants improves due to the higher production rate of $SO_4^{\cdot-}$ (Zhang et al., 2014; Wang et al., 2022). For enhanced activation, an examination was conducted to observe the impact of varying light intensities (i.e. 1, 2, 3 and 4 kw/m^2). The findings in Fig. 2(a-c) demonstrate a notable correlation between heightened light intensity and increased system temperature. When subjected to sunlight with an intensity of 4 kW/m^2, resulting in the highest rate of water evaporation compared to other light intensities. A comprehensive overview of the temperature variations during the experiment can be found in Fig. S2(a). Consequently, the light intensity resulting in the greatest temperature rise (4 kW/m^2) was chosen for implementation in the subsequent experiment.

Then, the temperature and evaporation rate of magnetic nanofluids with different Fe_3O_4 contents (i.e. 0.05, 0.1, 0.3 and 0.5 wt%) was evaluated, designated as Fe_3O_4–0.05, Fe_3O_4–0.1, Fe_3O_4–0.3, Fe_3O_4–0.5. As illustrated in Fig. 2(d-F), the temperature of Fe_3O_4–0.3 reached 57.2 ℃, achieving an evaporation rate of 1.412 kg/(m^2·h), which is fifteen times higher than that under dark condition. The detailed calculation process can be found in Text S1. Notably, the maximum rise in temperature of the nanofluids was 10.5 °C higher than that of the base fluid. Fig. S2(b) provides a detailed depiction of the temperature increase over time, illustrating the thermal behavior throughout the experiment. These findings indicate that the incorporation of Fe_3O_4 nanoparticles significantly enhanced the light absorption properties. The evaporation efficiency of Fe_3O_4–0.3 was 53.9 % greater than that of pure water. It is also evident that higher concentrations of Fe_3O_4 in the system correlate with a greater temperature rise, which can be attributed to the formation of an evaporation interface in the volumetric absorber. Furthermore, the water collection performance with different concentrations of Fe_3O_4 in nanofluids under 4 kw/m^2 light intensity was studied to assess the recovery efficiency of system in vaporized water. The weight change of water vapor in air is shown in Fig. S3. It can be seen that the water collection efficiency of all samples exceeded 90 % showing that the system exhibits excellent water vapor recovery performance.

2.3. Desalination and wastewater treatment

To verify the feasibility of V-SIE system integrating nanofluids and PDS for the treatment of highly saline organic wastewaters, batch experiments of RhB degradation were conducted in various comparative oxidation systems (including Light, Light/Fe_3O_4 and Light/Fe_3O_4/PDS processes). Fig. 3(a) demonstrates a clear decline in the RhB concentration over time when subjected to the simulated sunlight. This reduction was attributed to the breakdown of RhB by the ultraviolet rays present in sunlight. In contrast, the concentration of RhB initially decreased before subsequently increasing with the introduction of Fe_3O_4 NPs, exhibiting a lower degradation efficiency compared to direct sunlight irradiation. The described behavior can be attributed to the presence of Fe_3O_4 NPs, which create an interface for solar evaporation. Water evaporation during the experiment led to an increase in RhB concentration, as shown in Fig. S4. This interface obstructed the transmission of sunlight and reduced the efficiency of removing RhB, as shown in Fig. 3(b-c). Additionally, the temperature gradually rose with the increase of irradiation time, improving the evaporation performance and gradually increasing RhB concentration in the system.

It can be seen from Fig. 3(d) that at a concentration of 0.3 wt% of Fe_3O_4 nanofluids, light can only penetrate to a depth of 0.4 cm, forming the evaporation interface on the upper surface of the absorber. In contrast, light was not fully absorbed even at a depth of 10 cm within the absorber without Fe_3O_4 nanofluids. Importantly, the introduction of PDS led to a substantial reduction in RhB concentration in the V-SIE system, as shown in Fig. 3(a). RhB was almost completely degraded with its concentration decreasing from 100 mg/L to 1.5 mg/L after 3 h This finding further emphasized that the activation of peroxydisulfate via nanofluid-based V-SIE significantly enhanced the purification of high-salinity organic wastewater.

The effect of different concentrations of PDS on the removal of

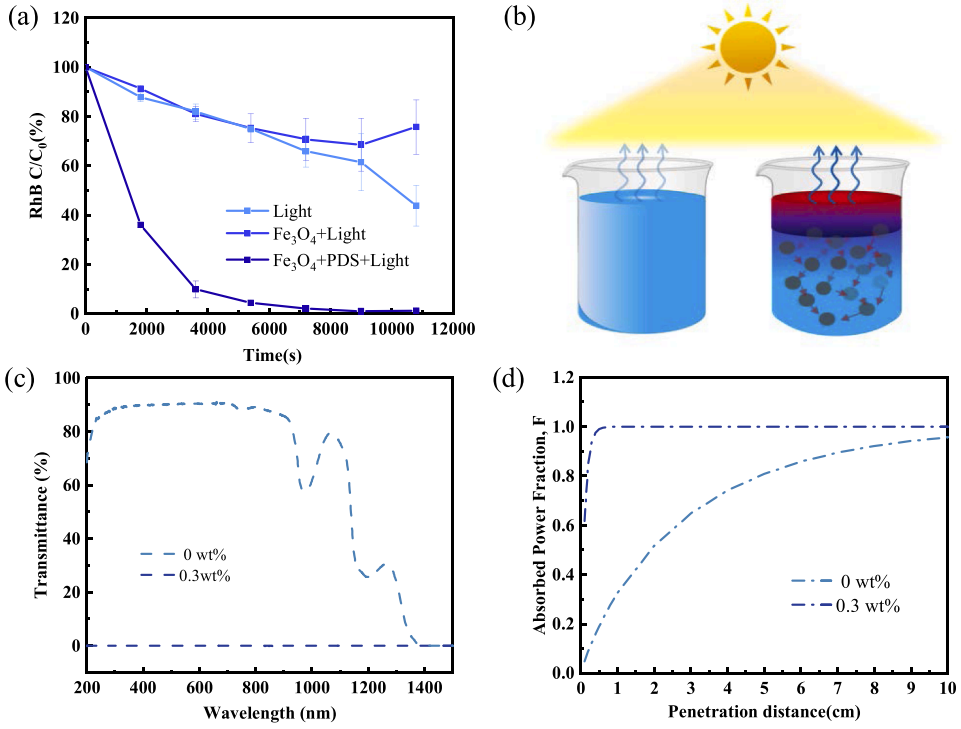

Fig. 3. . Content of RhB in different oxidation systems under light (a), Conditions: [RhB] = 0.1 g/L, [PDS] = 0.05 g/L, [Fe_3O_4] = 0.3 wt%, Time = 3 h; schematic of the solar evaporation interface in a volumetric absorber (b); transmittance spectra (c) and absorption power fraction (d) of fluids with and without Fe_3O_4 NPs.

pollutants in V-SIE system is shown in Fig. 4(a-b). The removal rate of RhB increased from 24.3 % to 99.4 % when the PDS concentration increased from 0 g/L to 0.1 g/L. It is observed that increasing the PDS concentration markedly raised k_{obs}, with a 22-flod increased in k_{obs} along with the increase of PDS concentration from 0 g/L to 0.1 g/L (Fig. 4(c)). Since the removal efficiency of RhB could reach 98.8 % within 3 h when the concentration of PDS was 0.05 g/L. Therefore, 0.05 g/L was selected as optimal PDS concentration at which the majority of contaminant can be removed completely and the chemical dosage was saved.

The degradation of RhB in high-salt wastewater at different concentrations of NaCl (i.e. 1 wt%, 3 wt%, and 10 wt%) were assessed Fig. 4 (d-e). In 0.3 wt% Fe_3O_4—H_2O nanofluids, RhB could be completely removed within 3 h at a light intensity of 4 kW/m^2, and the fastest degradation rate was obtained in wastewater containing 10 wt% salt. Under dark conditions, the degradation of RhB was more pronounced with higher NaCl concentrations, which was consistent with the

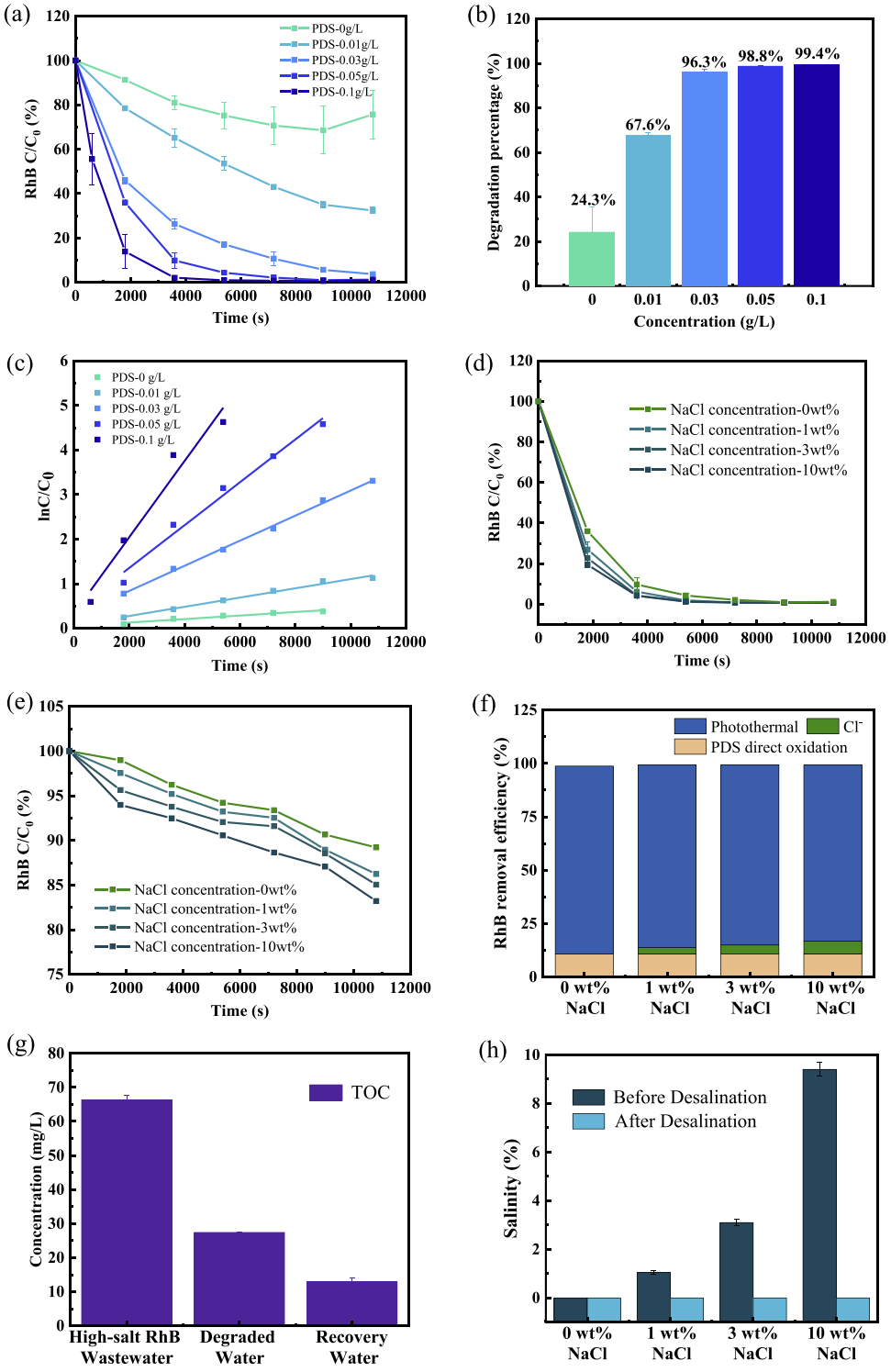

Fig. 4. Degradation process (a), removal efficiency (b), pseudo-first order rate (c) of RhB solutions containing different concentrations of PDS. Degradation process of RhB solutions containing different concentrations of NaCl under solar irradiation (d) and under dark (e); the roles of thermal effect, direct PDS oxidation, and Cl^- in facilitating the degradation of RhB by PDS (f); variation of TOC (g) and COD (h) concentrations and salinity of the water before and desalination (i).

conclusions under light regulation. This result can be attributed to the interaction of chloride ions (Cl^-) with sulfate radicals ($SO_4^{\cdot-}$) and hydroxyl radicals (·OH), resulting in the formation of chlorine radicals (·Cl) and chlorinated hydroxyl radicals (·ClOH), which further facilitated the degradation of pollutants (Li et al., 2022; Wang and Wang, 2018).

Additionally, the roles of thermal effect, chlorine, and direct PDS oxidation in the degradation of RhB were investigated. Fig. 4(f) illustrates that the contribution to RhB degradation increased progressively by rising NaCl concentration. Fig. 4(g) illustrates the variation of TOC after treatment in the system. The TOC concentration decreased by 58.6 %, resulting in a TOC concentration of only 12.9 mg/L in the recovery water. This indicates that the system is effective in removing organic pollutants in a high-salt environment. Additionally, the salinity of recovery water was not detectable (Fig. 4(h)), showing that V-SIE system also demonstrated excellent desalination performance.

2.4. Mechanisms of RhB degradation

2.4.1. Determination of radical species

The oxidative radicals responsible for RhB degradation were further examined using an EPR. As shown in Fig. 5(a-c), the EPR signals revealed the presence of $SO_4^{\cdot-}$, ·OH, $O_2^{\cdot-}$, and $^1O_2$. Notably, the black curve for Dark + Fe_3O_4 did not show any distinct characteristic peaks, suggesting that no active species were generated. In contrast, the Dark + Fe_3O_4 + PDS system (blue curve) displayed the emergence of $SO_4^{\cdot-}$ and ·OH, $O_2^{\cdot-}$ and $^1O_2$, which can be attributed to the catalytic activation of PDS (Wang and Wang, 2021). Fe_3O_4 NPs effectively promoted the generation of reactive species from PDS, leading to the degradation of RhB even without light (Fig. 5(d)). Upon the introduction of light, the peak intensities corresponding to all free radicals (red curve) were significantly higher than those in the Dark + Fe_3O_4 + PDS system (blue

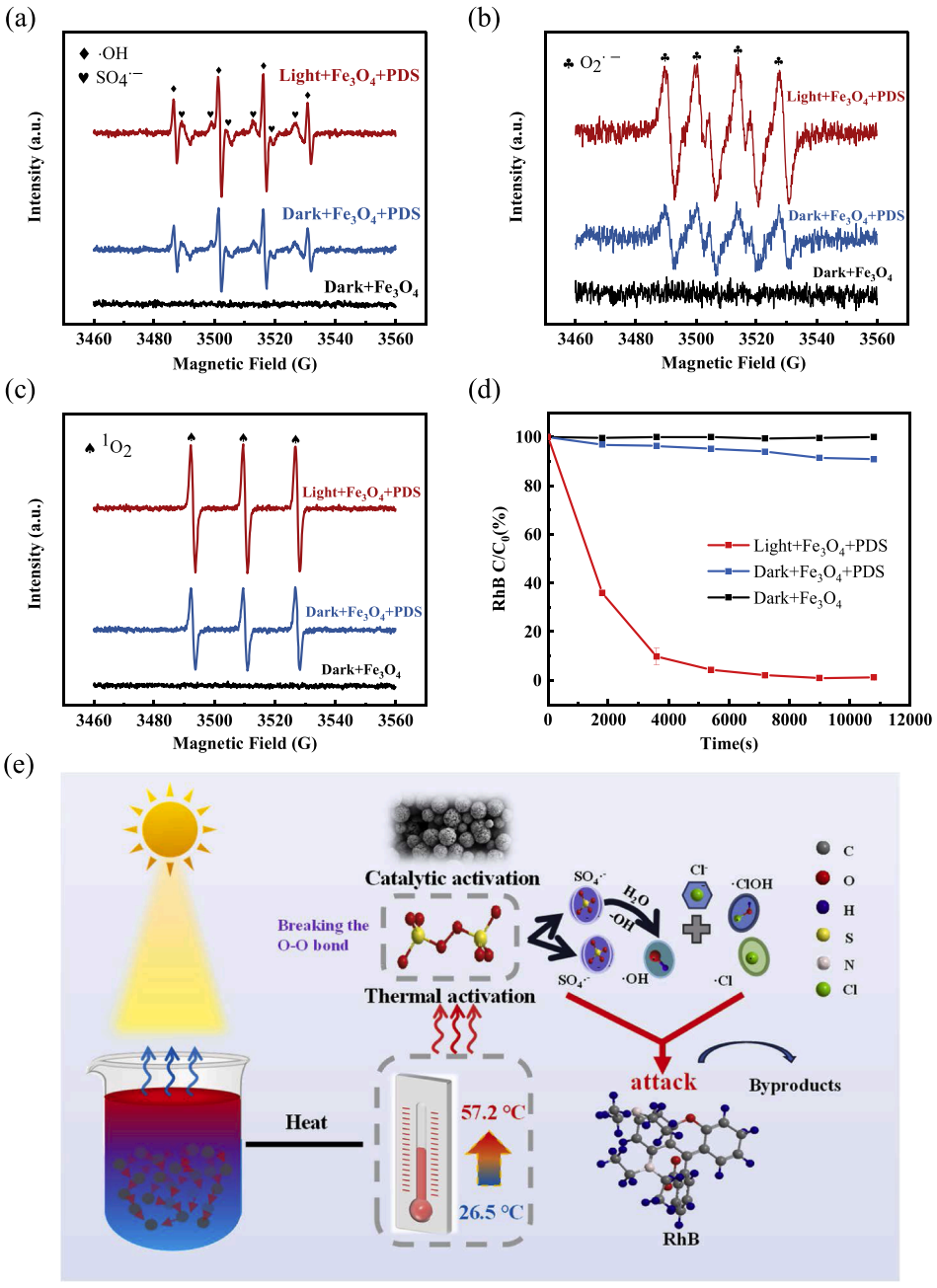

Fig. 5. EPR spectra of DMPO-$SO_4^{\cdot-}$ and DMPO-·OH (a) EPR spectra of $O_2^{\cdot-}$ radicals (b) and EPR spectra of $^1O_2$ (c) and content of RhB (d) under different conditions; the possible mechanisms for RhB decomposition using V-SIE system (e).

curve). This increase can be primarily attributed to the thermal effect of light, which enhanced PDS activation and further accelerated pollutant degradation, as shown in Fig. 5(e). The nanofluid containing 0.3 % Fe_3O_4 NPs formed an efficient solar energy absorption interface under sunlight. The interface absorbed a significant amount of sunlight and effectively converted it into thermal energy, thereby maintaining high evaporation efficiency. Meanwhile, the exceptional thermal conductivity of Fe_3O_4 NPs further heated the fluid beneath the absorber, providing the necessary thermal energy for PDS activation. This process stimulated PDS to generate more radicals, which play a crucial role in degrading pollutants.

2.4.2. *Possible degradation pathway*

The degradation pathway of pollutants was determined using LC-MS and the primary degradation intermediates are listed in Table S1. The degradation pathways of RhB mainly include four main stages: N-de-ethylation, chromophore cleavage, ring-opening, and mineralization, as illustrated in Fig. 6.

Initially, the progressive de-ethylation of the central carbon of RhB occurred due to continuous attack by free radicals. This process produced intermediate products with *m/z* value of 415, 387 and 359, corresponding to *N*-de-ethylated forms of RhB, namely *N,N*-diethyl-*N*'-ethylrhodamine, *N,N*-diethylrhodamine, *N*-ethyl-*N*'-ethylrhodamine, *N*-ethylrhodamine, respectively. Subsequent degradation of these *N*-de-ethylated intermediates resulted in additional intermediates with an *m/z* value of 331. These intermediate products lost 28 mass-to-charge ratios sequentially, leading to chromophore cleavage and the formation of benzene ring compounds like phthalic acid (*m/z* = 165), 2,4-dihydroxybenzoic acid (*m/z* = 155), salicylic acid (*m/z* = 137), and benzoic acid (*m/z* = 123). Subsequently, these compounds could decompose into smaller molecules, such as succinic acid (*m/z* = 118), malonic acid (*m/z* = 90), and propionic acid during the ring-opening stage. Ultimately, these intermediates can undergo further degradation, resulting in the formation of fully mineralized products such as CO_2 and H_2O, thereby

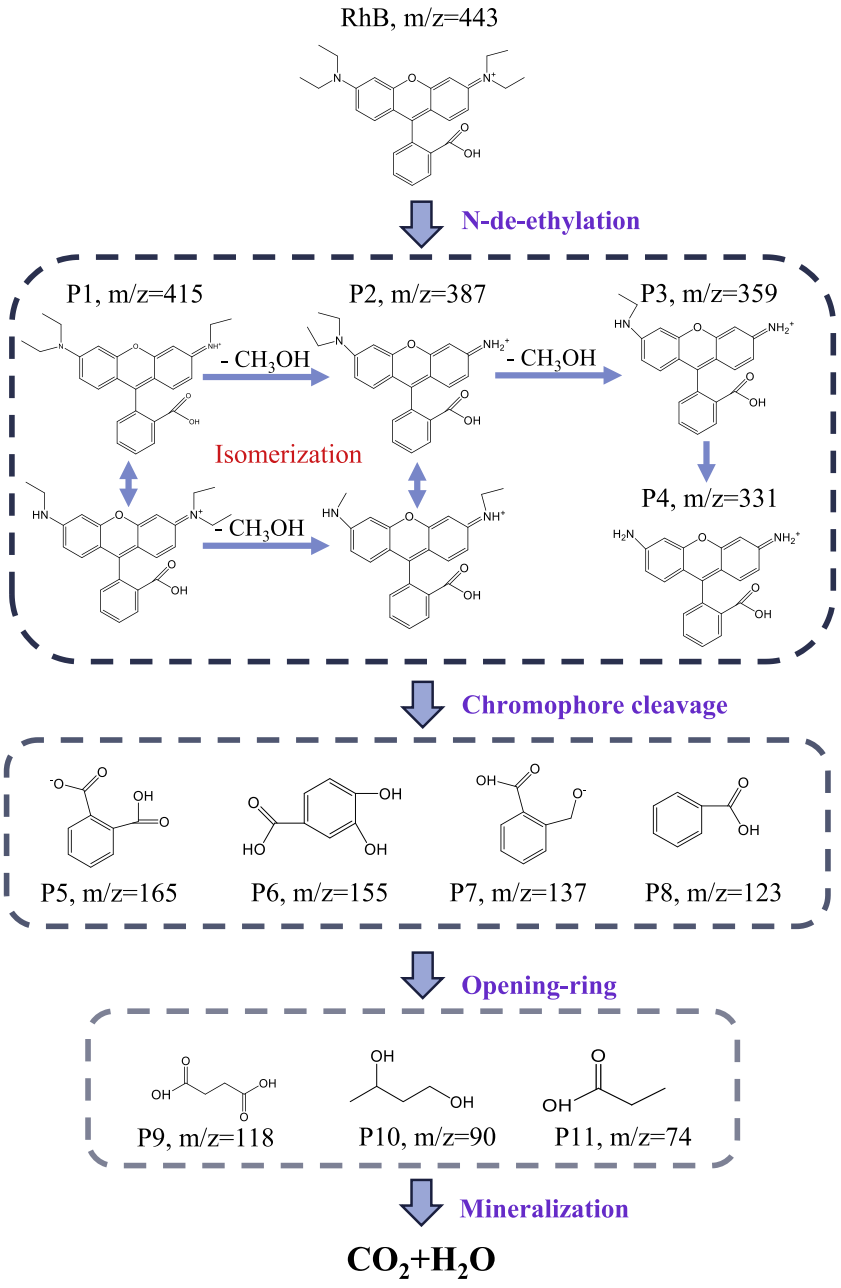

Fig. 6. Possible degradation pathway of RhB in the system.

completing the decomposition process. These findings are consistent with the previous research (Liu et al., 2022; Deng et al. 2023).

2.5. Reusable performance

As shown in Fig. S5(a), the aggregated Fe_3O_4 NPs at the bottom of the absorber after evaporation were subsequently rinsed multiple times with deionized water, and then separated from the water using a magnet for reusing. Fig. S5(b) shows that the Fe_3O_4—H_2O nanofluids achieved a significant temperature rise (up to 55 ℃) and exhibited excellent recyclability, with the removal efficiency of RhB consistently exceeding 99 % after eight cycles. Also, the steady, high-saturation magnetization of used Fe_3O_4 implied great ferromagnetic behavior (Fig. S5(c)), and the negligible changes to the morphology of Fe_3O_4 (Fig. S5(d)) indicated the good reusability and stability of Fe_3O_4 in the present work, which showed the potential for the practical application of this compound during wastewater treatment.

3. Conclusions

In this study, to achieve effective in-situ treatment of high-salt organic wastewater and obtain clean water, a volumetric solar interfacial evaporation (V-SIE) system integrating nanofluids and PDS was developed. The results indicate that the system achieved a temperature increase of 57.2 ℃, an evaporation rate of 1.412 kg/(m^2·h) and an impressive solar efficiency of 93.75 %. The rise in reaction temperature resulted in the homolytic cleavage of the O–O bond in PDS, generating $SO4^{\cdot-}$ and ·OH radicals, thereby enhanced the thermocatalytic degradation of RhB. The system enhances performance by promoting water evaporation and simultaneously providing energy for PDS activation. The removal efficiency of RhB reached 98.8 % within 3 h when the concentration of PDS was 0.05 g/L. This method can rapidly remove RhB in high-salt wastewater with excellent reusability and regeneration properties. Moreover, and the degradation efficiency of RhB in the system was not significantly reduced after consecutive 8 cycles. This study paves the path for using solar energy for high-salt organic wastewater treatment and water recovery.

4. Materials and methods

4.1. Chemicals and materials

Ferric chloride ($FeCl_3$·$6H_2O$), ethylene glycol ($C_2H_6O_2$), polyethylene glycol-400 (PEG-400) and ethanol (C_2H_5OH) were purchased from Macklin Biochemical Technology Co., Ltd, Shanghai, China. Urea ($(NH_2)_2CO$), PDS ($N_2S_2O_8$) and NaCl were supplied by Sinopharm Chemical Reagent Co. Ltd., Shanghai, China. All chemical reagents were analytical grade without further purification.

4.2. Preparation of nanofluid-based volumetric solar evaporation interface

Fe_3O_4 NPs were synthesized as illustrated in Fig. S6. Firstly, $FeCl_3$·$6H_2O$ (9.58 g) was dissolved in 250 mL of ethylene glycol and magnetically stirred to obtain the homogeneous suspensions. Subsequently, urea (16.66 g) and PEG-400 (16.66 g) were added to the solution individually, followed by magnetic stirring for 30 min to ensure complete dissolution and obtain a homogeneous mixture. The solution (240 mL) was transferred to polytetrafluoroethylene dilution reaction kettle (300 mL), and maintained at 200 °C for 20 h The product was separated via centrifugation once the reaction kettle cooled to room temperature. The separated product was then moved to a beaker, thoroughly washed with distilled water and ethanol, and dried at 60 °C for 3 h

The prepared Fe_3O_4 NPs were added into wastewater according to a certain proportion. Then, through ultrasonic treatment, the magnetic Fe_3O_4 NPs were evenly and stably dispersed in the wastewater to form Fe_3O_4—H_2O nanofluid-based volumetric solar evaporation interface with mass fractions of 0.05 %, 0.1 %, 0.2 %, 0.3 %, respectively.

4.3. Characterization

The surface features of materials were analyzed using a scanning electron microscope (SEM, ZEISS Gemini 300, Germany), while transmission electron microscopy (TEM, FEI Talos F200S, Netherlands) was employed to observe the sample morphology. The phase structures of Fe_3O_4 were analyzed through X-ray diffraction (XRD, Bruker-D8 Advance, Germany) to determine their crystallinity. The magnetic characteristics of the Fe_3O_4 magnetic NPs were measured using a vibrating sample magnetometer (VSM, Lakeshore 7404, USA). The optical properties were measured using an ultraviolet-visible-near infrared spectrophotometer (UV–Vis-NIR, Shimadzu 3600 plus, Japan) at room temperature. Reactive oxidation species (ROS) were monitored using electron paramagnetic resonance (EPR, Bruker-EmxPlus, Germany). The intermediates of RhB were analyzed by the liquid chromatography mass spectrometry (LC-MS, Agilent 1290II, USA).

4.4. Evaluation of evaporation and purification

4.4.1. Experimental setup

Experimental setup diagram is shown in Fig. S7. A xenon-arc lamp (Zolix Co.), covering a wavelength range of 200 – 2500 nm, was utilized to simulate sunlight, delivering a spectrum akin to that of natural sunlight as specified in ASTM G173–23 standards (ASTM, 2023). On the liquid surface, the radiation intensity was regulated by modifying the height of sample to change the distance between liquid surface and light source. The intensity of illumination was monitored by using a CEL-NP 2000–10 optical power meter (Beijing Zhongjin Educational Lighting Co., Ltd., China). Temperature variations were monitored using thermocouples throughout the test process. All the experiments were performed in a crystallizing dish with a diameter of 70 mm at 27 °C. This system also designed a water recovery unit, where water vapor passes through a collection device into the condenser tube (condensate was controlled at about 12 °C), resulting in clean recovery water.

4.4.2. Evaluation of evaporation

The evaporation test was performed at 27 ± 2 °C with a relative humidity of 60 %. Changes in water mass due to evaporation were measured using a high-precision analytical balance, with data automatically recorded by a computer every 30 s. The evaporation rate was calculated by Eq. (1) (Li et al., 2022).

$$\text{Evaporation rate}\left(\text{kg}/\left(m^2\,\text{h}\right)\right)=\frac{m_t}{S\cdot t} \tag{1}$$

where, m_t is the change in water mass (kg), S is the sample surface area (m^2), and t is the evaporation time (h).

For solar steam generation, the efficiency of converting solar energy to vapor (η) can also be interpreted as the ratio of evaporation heat to t solar radiation. It can be calculated by Eq. (2) (Yang et al., 2019; Zhang et al., 2016).

$$\eta=\frac{\dot{m}h_{LV}}{P_{in}} \tag{2}$$

where, $\dot{m}$ is the light-induced evaporation rate (kg/(m^2·h)), h_{LV} is the total enthalpy of water evaporation (kJ/kg), P_{in} is the incident solar irradiation power (kW/m^2).

The total enthalpy needed for water evaporation consists of both sensible and latent heat, each of which changes with temperature. This relationship is described by Eq. (3) (Wang et al., 2022; Liu et al., 2019).

$$h_{LV}=L_v+C(T-T_0) \tag{3}$$

$$L_V(\mathrm{T}) = 1.91846 \times 10^3 [T/(T - 33.91)]^2 \quad (4)$$

where, L_V is the enthalpy of water evaporation (kJ/kg), C is the specific heat capacity of water (4.18 kJ/kg), T *(K)* is the temperature at which vaporization occurs, and T_0 is the initial temperature of the water.

4.4.3. Evaluation of water collection efficiency

A precision analytical scale was utilized to track the changes in mass within the collecting beaker. The data was automatically captured by a computer at 30 s intervals. The water collection efficiency was calculated using Eq. (5).

$$\text{Water collection efficiency } (\%) = \frac{m_c - m_0}{m_t} \quad (5)$$

where, m_c is the weight of collected water (kg), m_0 is the weight of water vapor in air (kg), m_t *is* the weight of water evaporated (kg).

4.4.4. Evaluation of purification efficiency

The Total organic carbon (TOC) was detected by TOC-L CPN carbon analyzer (Shimadzu, Japan). The concentration of RhB was assessed by measuring its absorbance at the peak wavelength of 554 nm using a UV1900 UV–vis spectrometer (Beijing Purkinje General, China). Standard curve, which plot absorbance (A) against concentration (C), which is shown in Fig. S8. The residual concentration of RhB can be calculated using Eq. (6):

$$C_{RhB} = 65.203 UV_{554} + 0.4348 \quad (6)$$

where, C_{RhB} is the concentration of residual RhB and UV_{554} is the absorbance value of RhB at 554 nm.

The degradation of RhB is well-represented by a pseudo-first-order kinetics model, as illustrated by the following equation (Eq. (7)).

$$-\frac{d[RhB]}{dt} = k_{obs}[RhB] \quad (7)$$

where, k_{obs} denotes the pseudo-first-order rate constant, [RhB] represents the residual concentration of RhB at reaction time *t*. In addition, we measured the solution's salinity using a salinity meter (Jingcheng, SZSA, China).

CRediT authorship contribution statement

Chenqi Zhu: Writing – original draft, Investigation, Data curation. **Debing Wang:** Writing – review & editing, Investigation. **Shiying Bu:** Writing – review & editing. **Zhichao Wu:** Supervision. **Jie Zhang:** Writing – review & editing, Supervision, Project administration, Conceptualization. **Qiaoying Wang:** Writing – review & editing, Resources, Funding acquisition.

Declaration of competing interest

The authors declare that they have no known competing financial interests or personal relationships that could have appeared to influence the work reported in this paper.

Acknowledgements

The authors are grateful for the financial support from National Natural Science Foundation of China (52370045 & 51838009), and Natural Science Foundation of Shanghai (23ZR1467500).

Supplementary materials

Supplementary material associated with this article can be found, in the online version, at doi:10.1016/j.wroa.2024.100293.

Data availability

No data was used for the research described in the article.

References

ASTM, 2023. In: Standard Tables for Reference Solar Spectral Irradiances: Direct Normal and Hemispherical on 37° Tilted Surface: ASTM G173-23. USA.
Arshad, N., Irshad, M.S., Alomar, M., et al., 2023. Exploring perovskite oxide for advancing salt-resistant photothermal membranes and reliable thermoelectric generators. Chem. Eng. J. 475, 14. https://doi.org/10.1016/j.cej.2023.146200.
Chen, K., Li, L.X., Li, B.C., et al., 2024. Simultaneous fresh water collection and Li^+ selective adsorption enabled by a salt-resistant separated solar evaporator. Adv. Funct. Mater., 2402221 https://doi.org/10.1002/adfm.202402221.
Chen, G., Liu, R.X., Shon, H.K., et al., 2017. Open porous hydrophilic supported thin-film composite forward osmosis membrane via co-casting for treatment of high-salinity wastewater. Desalination 405, 76–84. https://doi.org/10.1016/j.desal.2016.12.004.
Chen, R., Zhang, T.Q., Kim, J., et al., 2021. Interfacial solar distillation for freshwater production: fate of volatile and semivolatile organic contaminant. Environ. Sci. Technol. 55 (9), 6248–6256. https://doi.org/10.1021/acs.est.0c07191.
Canh, N.V., Hang, N.T.N., Cuong, N.T., et al., 2024. Carbon nanodots-based interfacial nanofluid for high-performance solar-driven water evaporation. Diam. Relat. Mater. 149, 7. https://doi.org/10.1016/j.diamond.2024.111551.
Chen, H., Zhan, L.X., Gu, L.Y., et al., 2022. Fate and distribution of mercury during the desulfurization wastewater evaporation process. Fuel 318, 13. https://doi.org/10.1016/j.fuel.2022.123609.
Dao, V.D., Vu, N.H., Yun, S.N., 2020. Recent advances and challenges for solar-driven water evaporation system toward applications. Nano Energy 68, 18. https://doi.org/10.1016/j.nanoen.2019.104324.
Deng, S.M., Yang, M.L., An, Q., et al., 2023. Efficient rhodamine B dye degradation by red mud-grapefruit peel biochar catalysts activated persulfate in water. Environ. Sci. Pollut. Res. 30 (56), 119034–119049. https://doi.org/10.1007/s11356-023-30537-1.
Djellabi, R., Noureen, L., Dao, V., et al., 2021. Recent advances and challenges of emerging solar-driven steam and the contribution of photocatalytic effect. Chem. Eng. J. 431, 13. https://doi.org/10.1016/j.cej.2021.134024.
Forouzesh, M., Ebadi, A., Abedini, F., 2021. Thermocatalytic persulfate activation for metronidazole removal in the continuous operation. Sep. Purif. Technol. 258, 7. https://doi.org/10.1016/j.seppur.2020.118055.
Irshad, M.S., Arshad, N., Asghar, M.S., et al., 2023. Advances of 2D-Enabled Photothermal Materials in Hybrid Solar-Driven Interfacial Evaporation Systems toward Water-Fuel-Energy Crisis. Adv. Funct. Mater. 33 (51), 30. https://doi.org/10.1002/adfm.202304936.
Hu, L.M., Wang, P., Liu, G.S., et al., 2020. Catalytic degradation of *p*-nitrophenol by magnetically recoverable Fe_3O_4 as a persulfate activator under microwave irradiation. Chemosphere 240, 10. https://doi.org/10.1016/j.chemosphere.2019.124977.
He, H., Xiao, H., Liu, C.R., et al., 2023a. Efficient degradation of tetracycline with N-rGO/CuO catalysts under high salinity condition via persulfate activation dominated by non-radical pathways. Sep. Purif. Technol. 327, 11. https://doi.org/10.1016/j.seppur.2023.124936.
He, P.P., Lan, H.Y., Bai, H.Y., et al., 2023b. Rational construction of "all-in-one" metal-organic framework for integrated solar steam generation and advanced oxidation process. Appl. Catal. B: Environ. 337, 14. https://doi.org/10.1016/j.apcatb.2023.123001.
Jia, Z.L., Li, F.Z., Zhang, X., et al., 2023. Effects of cation exchange membrane properties on the separation of salt from high-salt organic wastewater by electrodialysis. Chem. Eng. J. 475, 11. https://doi.org/10.1016/j.cej.2023.146287.
Liu, Z.X., Wu, B.H., Zhu, B., et al., 2019. Continuously producing waterstream and concentrated brine from seawater by hanging photothermal fabrics under sunlight. Adv. Funct. Mater. 29 (43), 11. https://doi.org/10.1002/adfm.201905485.
Liu, D.D., Tang, Y.B., Hao, Z.K., et al., 2022. Comparative study of H_2O_2/PDS-based advanced oxidation process using Fe_3O_4 nanoparticles for Rhodamine B degradation: mechanism, stability and applicability. J. Water. Process. Eng. 47, 13. https://doi.org/10.1016/j.jwpe.2022.102757.
Liu, L.J., Liu, H.J., Fan, Z.F., et al., 2024. Simultaneous solar-driven interfacial evaporation and photo-fenton oxidation by semiconducting metal–organic framework from waste polyimide. Energy Environ. Mater. 2024, 13. https://doi.org/10.1002/eem2.12812.
Li, J.B., Cui, Y.X., Xiu, H.J., et al., 2022a. An integrative cellulose-based composite material with controllable structure and properties for solar-driven water evaporation. Cellulose 29 (4), 2461–2477. https://doi.org/10.1007/s10570-022-04442-8.
Li, X.X., Song, C., Sun, B.B., et al., 2022b. Kinetics of zero-valent iron-activated persulfate for methylparaben degradation and the promotion of Cl. J. Environ. Manag. 321, 15. https://doi.org/10.1016/j.jenvman.2022.115973.
Liu, J., Wang, J.Q., 2024. Experimental study on the mechanism and efficiency of a closed-cycle low-temperature evaporation system for treating high salt and high organic matter wastewater. J. Water. Process. Eng. 58, 8. https://doi.org/10.1016/j.jwpe.2024.104926.
Mora, V.C., Rossoa, J.A., Le Roux, G.C., et al., 2009. Thermally activated peroxydisulfate in the presence of additives: a clean method for the degradation of pollutants.

Chemosphere 75 (10), 1405–1409. https://doi.org/10.1016/j.chemosphere.2009.02.038.
Meng, Z.G., Li, Z.L., Li, Y., et al., 2022. Novel nanofluid based efficient solar vaporization systems with applications in desalination and wastewater treatment. Energy 247, 10. https://doi.org/10.1016/j.energy.2022.123513.
Ngoc, N.T.B., Hoang, N.M., Hau, L.T., et al., 2024. Synthesis of Fe_3O_4/carbon dots for excellent water treatment applications. Inorg. Chem. Commun. 170, 8. https://doi.org/10.1016/j.inoche.2024.113254.
Nguyen, M.H., Ngoc, N.T.B., Huy, H.V., et al., 2023. Use of carbon materials for constructing a closed water treatment system. J. Power Sources 573, 6. https://doi.org/10.1016/j.jpowsour.2023.233111.
Qian, Y.J., Liu, X., Li, K., et al., 2020. Enhanced degradation of cephalosporin antibiotics by matrix components during thermally activated persulfate oxidation process. Chem. Eng. J. 384, 10. https://doi.org/10.1016/j.cej.2019.123332.
Qu, J., Tang, R., Cui, Q.Y., et al., 2023. Heat-transfer analysis of interfacial solar evaporation and effect of surface wettability on water condensation and collection. Int. J. Therm. Sci. 184, 14. https://doi.org/10.1016/j.ijthermalsci.2022.107911.
Ren, L.H., Chen, M., et al., 2021. Efficacy of a novel electrochemical membrane-aerated biofilm reactor for removal of antibiotics from micro-polluted surface water and suppression of antibiotic resistance genes. Bioresour. Technol. 338, 8. https://doi.org/10.1016/j.biortech.2021.125527.
Tram, N.A., Hien, N.T., Hoang, N.M., et al., 2023. Carbon dots in environmental treatment and protection applications. Desalination 548, 14. https://doi.org/10.1016/j.desal.2022.116285.
Trinh, V., Nguyen, N.A., Omelianovych, O., et al., 2022. Sustainable desalination device capable of producing freshwater and electricity. Desalination 535, 11. https://doi.org/10.1016/j.desal.2022.115820.
Wang, X.Z., He, Y.R., Liu, X., et al., 2017. Investigation of photothermal heating enabled by plasmonic nanofluids for direct solar steam generation. Sol. Energy 157, 35–46. https://doi.org/10.1016/j.solener.2017.08.015.
Wang, Y., Mei, X., Ma, T.F., et al., 2018. Green recovery of hazardous acetonitrile from high-salt chemical wastewater by pervaporation. J. Clean. Prod. 197, 742–749. https://doi.org/10.1016/j.jclepro.2018.06.239.
Wang, J.L., Wang, S.Z., 2018. Activation of persulfate (PS) and peroxymonosulfate (PMS) and application for the degradation of emerging contaminants. Chem. Eng. J. 334, 1502–1517. https://doi.org/10.1016/j.cej.2017.11.059.
Wang, T., Li, B.R., Wu, L.G., et al., 2019. Enhanced performance of TiO_2/reduced graphene oxide doped by rare-earth ions for degrading phenol in seawater excited by weak visible light. Adv. Powder Technol. 30 (9), 1920–1931. https://doi.org/10.1016/j.apt.2019.06.011.
Wang, J.L., Wang, S.Z., 2021. Effect of inorganic anions on the performance of advanced oxidation processes for degradation of organic contaminants. Chem. Eng. J. 411, 12. https://doi.org/10.1016/j.cej.2020.128392.
Wang, J.L., Wang, W.K., Li, J.G., et al., 2021. Universal strategy to prepare a flexible photothermal absorber based on hierarchical Fe-MOF-74 toward highly efficient solar interfacial seawater desalination. ACS Appl. Mater. Interfaces 13 (38), 45944–45956. https://doi.org/10.1021/acsami.1c11176.
Wang, D.B., Liu, Y., Wang, Q.Y., et al., 2022a. Activation of peroxydisulfate via photothermal synergistic strategy for wastewater treatment: efficiency and mechanism. J. Hazard. Mater. 436, 10. https://doi.org/10.1016/j.jhazmat.2022.129224.
Wang, Q.M., Qin, Y., Jia, F.F., et al., 2022b. Recyclable Fe_3O_4@Polydopamine (PDA) nanofluids for highly efficient solar evaporation. Green Energy Environ. 7 (1), 35–42. https://doi.org/10.1016/j.gee.2020.07.020.
Wang, J., Liu, H.B., Gao, Y., et al., 2022c. Pilot-scale advanced treatment of actual high-salt textile wastewater by a UV/O_3 pressurization process: evaluation of removal kinetics and reverse osmosis desalination process. Sci. Total Environ. 857, 10. https://doi.org/10.1016/j.scitotenv.2022.159725.
Wang, Y.M., Zhao, J.J., Zhang, Z.C., et al., 2023. Water strider inspired floating solar evaporator with high salt-resistant ability for desalination of contaminated seawater. J. Environ. Chem. Eng. 11 (3), 12. https://doi.org/10.1016/j.jece.2023.109800.
Yang, Y.W., Que, W.X., Zhao, J.Q., et al., 2019. Membrane assembled from anti-fouling copper-zinc-tin-selenide nanocarambolas for solar-driven interfacial water evaporation. Chem. Eng. J. 373, 955–962. https://doi.org/10.1016/j.cej.2019.05.099.
Zhang, X., Xu, X.W., Li, T.T., et al., 2014. Composite photothermal platform of polypyrrole-enveloped Fe_3O_4 nanoparticle self-assembled superstructures. ACS Appl. Mater. Interfaces 6 (16), 14552–14561. https://doi.org/10.1021/am503831m.
Zhang, C.B., Yan, C., Xue, Z.J., et al., 2016. Shape-controlled synthesis of high-quality Cu_7S_4 nanocrystals for efficient light-induced water evaporation. Small 12 (38), 5320–5328. https://doi.org/10.1002/smll.201601723.
Zhang, H., Du, Y.P., Jing, D.W., Yang, L., et al., 2023a. Integrated janus evaporator with an enhanced donnan effect and thermal localization for salt-tolerant solar desalination and thermal-to-electricity generation. ACS Appl. Mater. Interfaces 15 (42), 49892–49901. https://doi.org/10.1021/acsami.3c12517.
Zhang, H., Li, X.K., Liu, X.Y., et al., 2023b. Biomimetic hydrogel with directional heat regulation for efficient solar desalination. Chem. Eng. J. 473, 10. https://doi.org/10.1016/j.cej.2023.145484.